Chapter 5

Effects of Stratification on Biogenic Ocean Mixing via Drift

5.1 Introduction

Ocean dynamics differ from most classical fluid dynamics problems due to the stratified nature of the water column at depths whose length scales are on the order of kilometers. In the case of a stable stratification, less dense fluid lies above denser fluid. However, due to the dynamic nature of the ocean and processes that act to mix and disrupt constant surfaces of density (or isopycnals), unstably stratified regions in the ocean exist [87, 128]. Aside from physical mixing processes such as tidal flows, internal waves, and surface interactions with the atmosphere [89, 142, 117], a mixing process known as double-diffusive convection occurs via changes in physical properties of a stratified fluid [119, 130, 107]. Fluid density in an incompressible ocean is dependent on concentrations of salt and temperature. Due to different molecular diffusivities of these quantities, advective instabilities and transport (known as double-diffusive convection) can be achieved. The bulk of mixing in the oceans has been attributed to these processes. As mentioned in chapter 4, to maintain the thermohaline circulation, additional sources of mixing may be required to close the mixing energy budget [88]. Based on recent work in the field, biologically generated (or biogenic) mixing has the potential to contribute to mixing in the ocean [59, 35].

Recent measurements of biogenic mixing show an increase in dissipation rates in the vicinity of large populations of swimming animals [74]. Since animals inject turbulent kinetic energy at

length scales proportional to their size, limits of mixing extent due to wake structures are expected [127]. For small plankton, these length scales are greater than the Kolmogorov length scale and generally less than the Ozmidov length scale; turbulent fluid motions injected near these scales are depressed either by viscosity or buoyancy effects, respectively. Therefore, fluid characteristics limit the effectiveness of biogenic mixing if mixing is induced solely by the fluid structures created in an animal's wake [135]. A mechanism of fluid transport due to the pressure field generated by a swimming animal was later identified by measurements of flow around a jellyfish [67]. Unlike turbulent structures in animal wakes, this mechanism (called drift; [34, 41]) is enhanced by viscosity, thereby allowing for efficient stirring by small animals. This transport mechanism relies on fluid diffusion and other physical mixing processes to disrupt the stirred field and lead to chemical mixing [42]. In unstratified flows, simulations show that the drifting volume of fluid propagates with the body for as long as the body moves. However, the behavior of drift in a stratified flow, where buoyancy effects may limit the extent of the transport mechanism has not been investigated.

In order to determine the effects of stratified flow on the drift mechanism, we computed analytical solutions of the flow for a sphere moving in potential and Stokes (or creeping) flow [75, 6]. Using the Boussinesq approximation to decouple the effects of buoyancy on the simulated flow [138, 132], we determined the displacement of fluid particles from an equilibrium position (based on the fluid particle density and the ambient fluid density) as levels of stratification are varied. We show that the fluid transport due to drift in stratified flow conditions are altered; the characteristic length scale of the drift process does not scale with the distance of animal migration as previously thought [67]. However, due to the diffusive properties of fluid in the ocean, drift may play a role in enhancing diffusive transport by initiating these processes via stirring.

5.2 Computational Methods

5.2.1 Theoretical Simulations of Fluid Particle Displacements

The motion of fluid particles induced by the vertical translation of a sphere was simulated by advecting a horizontal row of particles according to the theoretical solution for flow around a sphere in potential (inviscid and irrotational) and Stokes (or creeping flow, non-inertial) flow. The streamfunction in polar coordinates for a moving sphere in potential flow [6] is

$$\Psi = -\frac{1}{2} U\, r^2 \sin^2\theta \left(1 - \frac{a^3}{r^3}\right), \tag{5.1}$$

where r is the radial coordinate, θ is the angular coordinate measured from the direction of oncoming flow (in the reference frame of the propagating sphere), U is the translational velocity of the sphere, and a is the sphere radius. The radial and tangential components of velocity (u_r and u_θ, respectively) can be found from the streamfunction in equation (5.1) by differentiating Ψ with respect to θ or r,

$$\begin{aligned} u_r &= \frac{1}{r^2 \sin^2\theta}\frac{d\Psi}{d\theta} = U\cos\theta\left(1 - \frac{a^3}{r^3}\right), \\ u_\theta &= -\frac{1}{r\sin\theta}\frac{d\Psi}{dr} = -U\sin\theta\left(1 + \frac{a^3}{2r^3}\right). \end{aligned} \tag{5.2}$$

The streamfunction for a moving sphere in Stokes flow [75] is

$$\Psi = U\, r^2 \sin^2\theta \left[\frac{1}{2} + \frac{a^3}{4r^3} - \frac{3a}{4r}\right], \tag{5.3}$$

and using equation (5.2) and the streamfunction in equation (5.3), we find the radial and tangential velocity components for Stokes flow to be

$$\begin{aligned} u_r &= U\cos\theta\left[1 + \frac{a^3}{2r^3} - \frac{3a}{2r}\right], \\ u_\theta &= -U\sin\theta\left[1 - \frac{a^3}{4r^3} - \frac{3a}{4r}\right]. \end{aligned}$$

Since we are interested in the displacement of fluid particles and the resulting drift volume of a body moving vertically, it is beneficial to convert from polar to cartesian coordinates using the coordinate conversion,

$$u_x = u_r \cos\theta - u_\theta \sin\theta,$$
$$u_y = u_r \sin\theta + u_\theta \cos\theta. \tag{5.4}$$

Streamlines for the simulated potential and Stokes flow cases are shown in figure 5.1.

To advect fluid particles in a simulated or measured flow, the following initial value problem needs to be solved

$$\frac{d\vec{x}}{dt} = \vec{u}, \tag{5.5}$$

with $\vec{x}\,(t_0) = \vec{x_0}$. The term $\vec{u}$ in equation (5.5) denotes fluid particle velocity at a given position $\vec{x}$ within the domain. An Eulerian solution of equation (5.5) gives solutions of the form $\vec{x_{n+1}} = \vec{x_n} + \vec{u}\Delta t$, where Δt corresponds to the time step in the simulation or $t_{n+1} = t_n + \Delta t$. A more precise method for explicitly solving equation (5.5) is the Runge-Kutta method with solutions,

$$\vec{x_{n+1}} = \vec{x_n} + \frac{1}{6}\,\Delta t\,(k_1 + 2\,k_2 + 2\,k_3 + k_4)\,,$$

where k_i corresponds to the estimated slope computed at different time intervals, and is dependent on the local velocity $\vec{u}$. The Runge-Kutta method is a fourth-order method such that the total accumulated error is on the order of Δt^4 [13].

To reduce the computational requirements to simulate these flows, the mean displacement of a finite number of fluid particles instead of the drift volume [67] is measured over time. As these particles are moved from their equilibrium position due to the moving sphere, the displacement of these particles are averaged. Figure 5.2 compares the mean displacement of advected fluid particles when using Eulerian or Runge-Kutta solutions of equation (5.5). We see that the mean displacement using the Eulerian solution is strongly dependent on time step Δt (or dt); solutions converge for

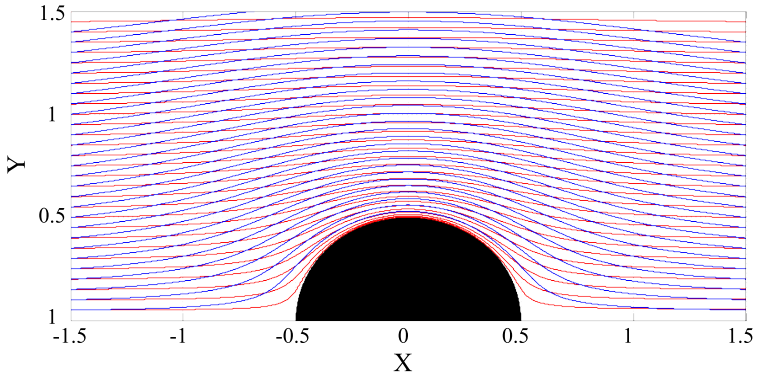

Figure 5.1. Simulated streamlines of flow over a sphere in potential (red curves) and stokes (blue curves) flow. Axes are in units of body diameters.

smaller dt using the Runge-Kutta method of integration. Therefore, for subsequent analysis, the Runge-Kutta time integration method will be used with time step $dt = 0.01$. To match convention in the oceanographic literature, the vertical axis will be defined as the z-direction such that $u_z = u_y$ from the previous equations.

5.2.2 Simulating a Stratified Fluid

To accurately investigate the impact that swimming animals have on mixing in the ocean, fluid transport dynamics need to be investigated in conjunction with physical properties of a fluid. Using the Boussinesq approximation to decouple effects of buoyancy from a simulated flow [138], the displacement of fluid particles due to a moving sphere is quantified. Since the degree of stratification in the ocean varies by several orders of magnitude depending on location and depth in the water column [128], simulation of the drift mechanism will be conducted at various stratification levels by varying the buoyancy frequency N.

To simulate a stratified fluid, a buoyancy acceleration (b) is defined to be parallel to the direction of gravitational acceleration g, which arises when the difference in the density of a fluid particle ($\rho_{particle}$) and surrounding ambient fluid ($\rho_{ambient}$) is nonzero, or $\Delta\rho = \rho_{particle} - \rho_{ambient} \neq 0$. Therefore, the buoyancy acceleration b is described by

$$b = -\frac{g}{\rho_0}\,\Delta\rho, \tag{5.6}$$

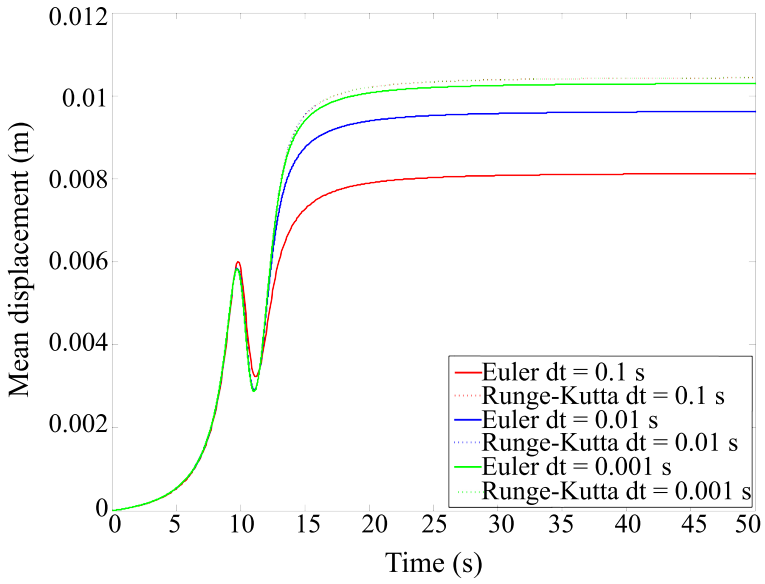

Figure 5.2. Comparison of mean particle displacement as the time step dt is decreased using Eulerian and Runge-Kutta particle advection. Solid lines indicate the Eulerian time-step solution and dashed lines indicate Runge-Kutta integration. As dt is decreased by two orders of magnitude, the mean displacement profile changes significantly using Eulerian particle advection. A noticeable change in the mean displacement profile is not observed using the Runge-Kutta integration technique.

where ρ_0 is the reference density [132]. Since the density of the fluid parcel is conserved (i.e., $\rho_{particle} = const$), the density of the surrounding fluid $\rho_{ambient}(z)$ is a function of buoyancy frequency N and depth z. Assuming that the flow is linearly stratified, the variation in density has a slope equal to $\frac{\rho_0}{g}N^2$ [138, 132]. Using equation (5.6), and ignoring the effects of buoyancy in the horizontal direction (since the quantity of interest is the vertical displacement of fluid particles), the vertical velocity component (u_z) of a fluid particle in a stratified flow is

$$u_z = u_{z,sphere} + u_{z,buoyancy} = u_{z,sphere} + \frac{b}{N}. \tag{5.7}$$

To advect fluid particles in stratified flow conditions, u_z will be used in equation (5.5) instead of u_y (where $y = z$ to match convention) in equation (5.4). For the stratified flow case, we enforce the condition that particles cannot enter the sphere by moving the fluid particle outside the body boundary by a distance defined by the particle displacement. The application of the Boussinesq approximation in the simulations is valid since the density perturbations are small (or $\Delta\rho/\rho_0 \gg 1$)

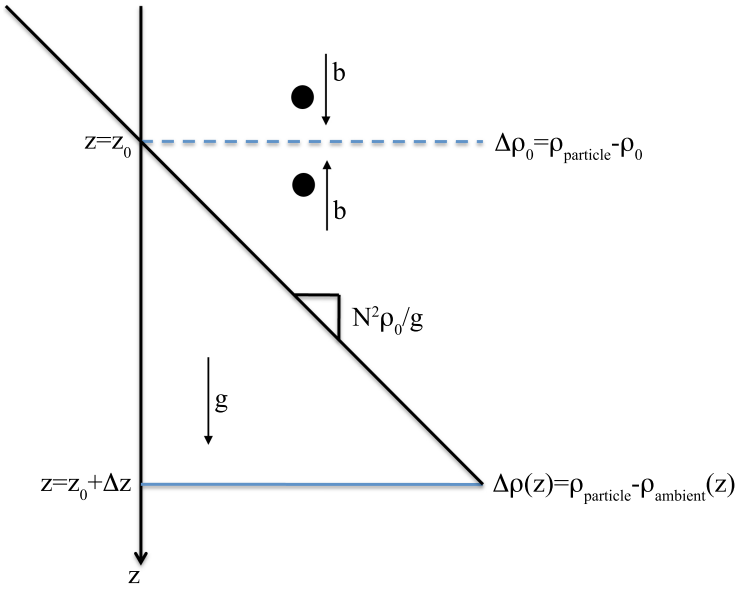

Figure 5.3. Diagram depicting the stratified simulations where $\Delta\rho$ is used to determine the buoyancy forcing (equation (5.6)) and has a constant linear slope of $N^2\,\rho_0/g$ with vertical distance z. In this diagram, gravitational acceleration is pointed downwards. In the case where $\rho_{particles} = \rho_{ambient}$ (or $\Delta\rho = 0$), the direction of the buoyancy force b varies depending on the location of the particle relative to the equilibrium position (or $z = z_0$) and is indicated by the two arrows.

and the body migration distances are much smaller than the ocean depth [138, 128, 132].

The ratio of mean particle displacement in the stratified ($X_{stratified}$) and unstratified ($X_{unstratified}$) case is a useful indicator of fluid transport in stratified conditions (figure 5.4). As the starting position of the spherical body relative to the initial particle location is increased (figure 5.4A), we see consistent behavior of long-term dynamics for starting positions greater than the equilibrium position (or $startpos = 0$). The mean particle displacement ratio converges to a single solution for grid mesh spacing $ds \geq 0.01$ (figure 5.4B). Therefore, the body starting position and grid mesh spacing will be 5 diameters upstream of the equilibrium position and 0.005 diameters, respectively for all simulations in this study.

5.3 Results

The accuracy of our potential flow simulations was confirmed by comparing the results for partial drift volume (or drift in finite fluid domains, V_{DP}; see figure 5.7) with the drift volume (in an infinite

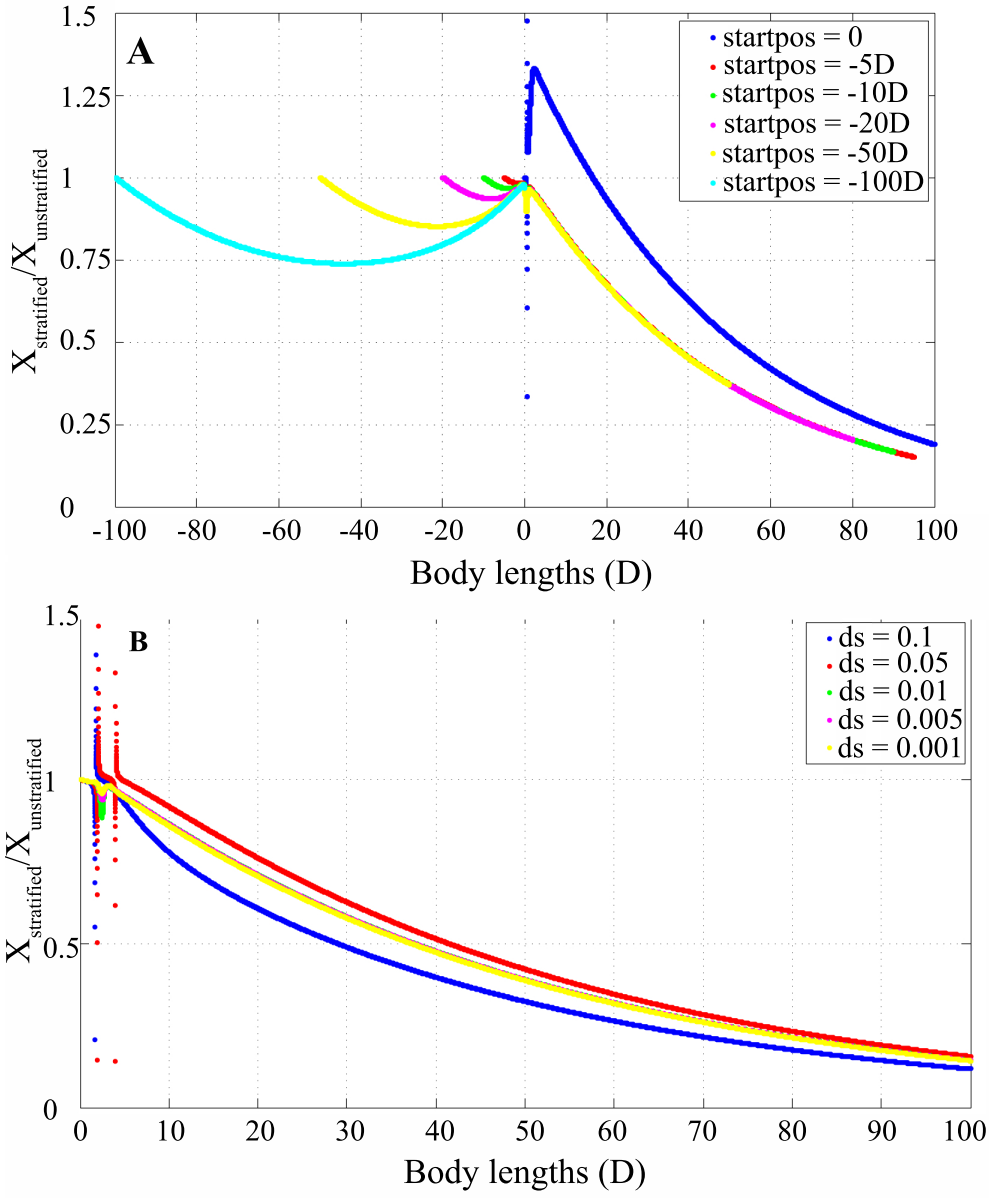

Figure 5.4. Comparison of mean particle displacement in stratified ($N = 1$ s^{-1}), potential flow ($X_{stratified}$) normalized by the mean particle displacement in unstratified flow ($X_{unstratified}$). The x-axis is in units of sphere body diameters D. A, As the starting position of the spherical body relative to the initial particle location is increased, we see consistent behavior of long-term dynamics for starting positions not at the initial particle location (or $startpos = 0$). B, The mean particle displacement ratio converges to a single solution for grid mesh spacing $ds \geq 0.01$. Negative values on the x-axis indicate starting positions upstream of the initial particle locations; positive values are downstream. For subsequent analysis, the body starting position will be $startpos = 5D$ and grid mesh spacing $ds = 0.005$.

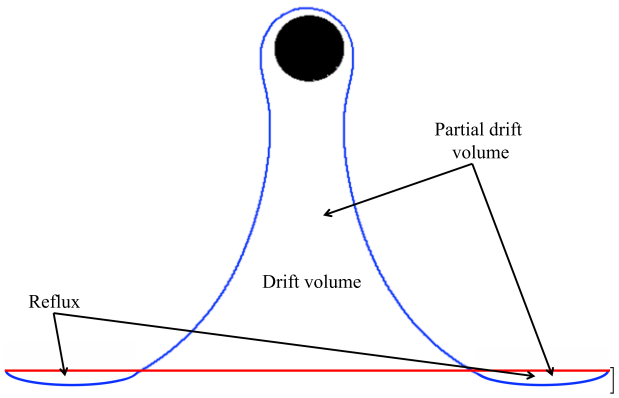

Figure 5.5. Diagram showing the partial drift volume in a finite control volume as defined by Eames et al. [39]. Red line indicates the initial location of fluid particles; blue line indicates the location of deformed fluid particles; black circle is the body (moving upwards). The reflux is the fluid bound by the deformed and initial material lines downstream of the initial fluid particle locations. The drift volume is the region of fluid bound by the upstream deformed material line and the initial material line. The partial drift volume includes the contributions from the reflux and drift volumes.

domain, V_D). Since the domain of our simulations are finite, the reported drift volume corresponds to the partial drift volume as defined by Eames et al. [39]. The ratio between the simulated partial drift V_{DP} and total drift V_D [39, 26] is given approximately by

$$\frac{V_{DP}}{V_D} \approx -\frac{1}{2} + \frac{3}{2\sqrt{1+(r_L/d_0)^2}}, \tag{5.8}$$

where r_L is the finite radius of the plane of fluid particles being advected and d_0 is the initial distance of approach between the propagating body and the particle plane. We see from figure 5.6, that r_L and d_0 correspond to 2 and 5 body diameters, respectively. Using the partial drift correction in equation (5.8), the drift volume ratio is 0.89. Figure 5.7 shows the asymptotic behavior of the ratio of partial drift volume to body volume (V_B) of the potential flow simulations. As the body moves downstream from the fluid particle plane, $V_{DP}/V_B \approx 0.45$. Using this ratio and the partial drift correction in equation (5.8), we find that the coefficient of added mass for a translating sphere ($C_{AM,sphere}$) is

$$C_{AM,sphere} = \frac{V_D}{V_B} = \frac{V_{DP}/V_B}{V_{DP}/V_D} \approx 0.5,$$

and the drift volume is recovered.

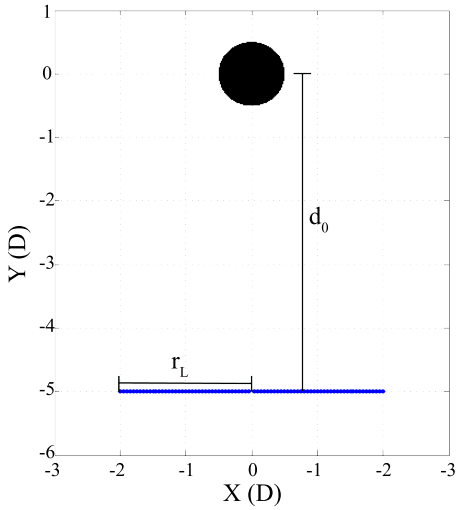

Figure 5.6. Initial conditions for the flow simulations where the finite radius of the plane of fluid particles r_L and initial distance of approach between the propagating body and the particle plane d_0 are 2 and 5 body diameters, respectively. The spherical body is moving downwards. The initial conditions are used to determine the partial drift correction (equation (5.8)) that relates the partial drift volume V_{DP} with the drift volume V_D.

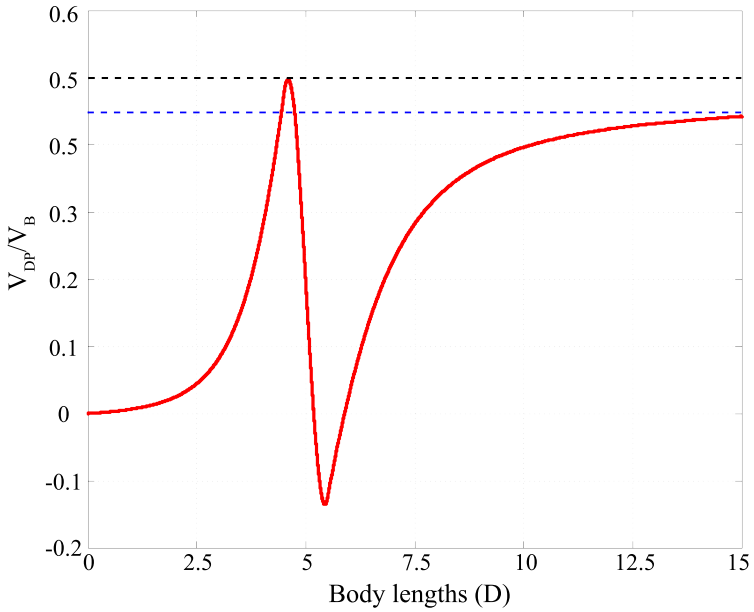

Figure 5.7. The variation of partial drift volume ratio (V_{DP}/V_B) as a sphere moves in potential flow (red) where V_{DP} is the partial drift volume and V_B is the volume of the sphere. The theoretical limit of the drift volume ratio (V_D/V_B) is 0.5, indicated by the dashed, black line. The asymptote for the partial drift simulation ($V_{DP}/V_B = 0.45$) is indicated by the dashed, blue line. Using the partial drift correction (equation (5.8); [41]), we recover the theoretical limit for a sphere moving in an infinite domain.

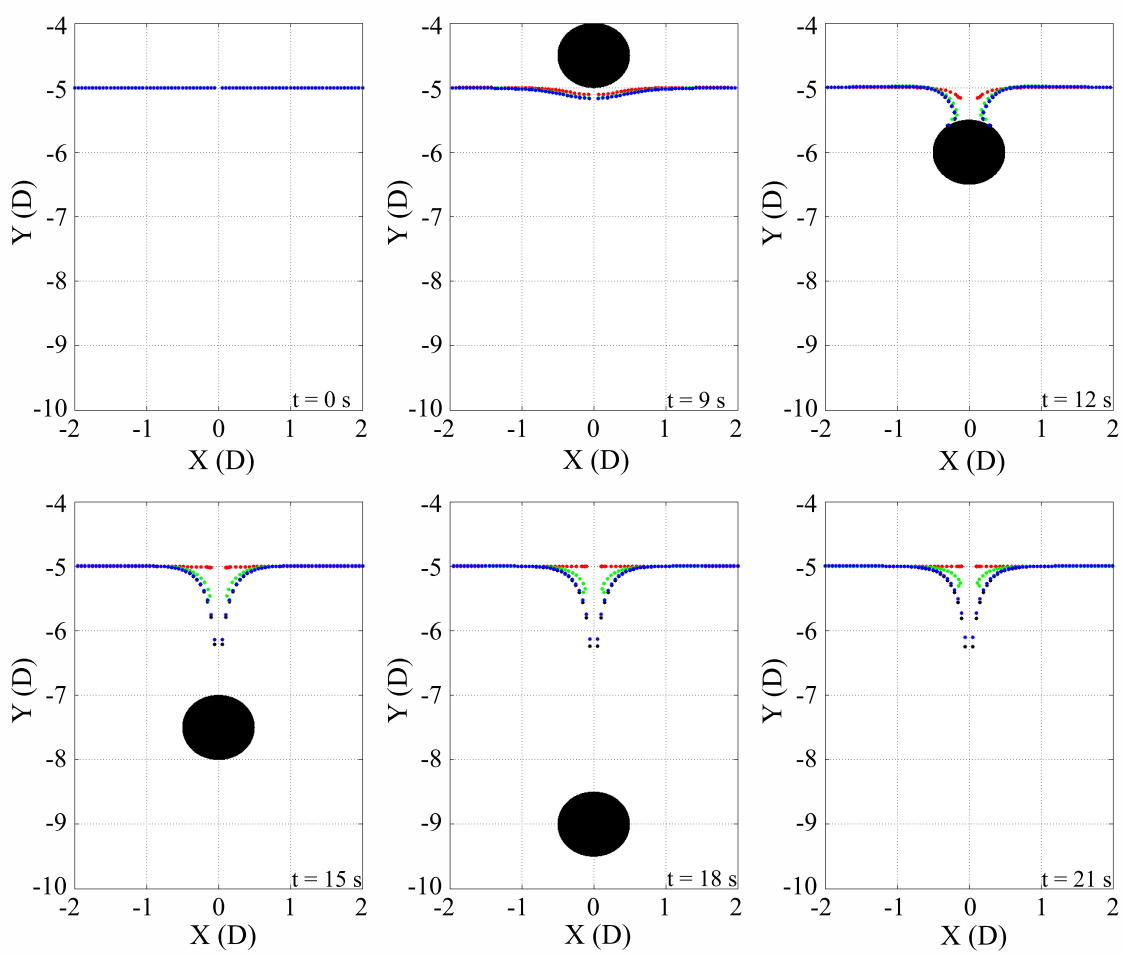

Figure 5.8. Displacement of fluid particles in potential flow due to a moving sphere. Black dots indicate fluid particles in unstratified flow conditions. Blue, green and red dots represent fluid particles in stratified flow with $N = 0.01$, $N = 0.1$, and $N = 1$ s^{-1}, respectively.

Figure 5.8 shows a time series of fluid particle positions due to the moving sphere in potential flow given unstratified and stratified flow conditions. As the sphere moves past the plane of fluid particles, the particles where $N = 1$ s^{-1} (red dots) return to the equilibrium position soon after the body passes through the plane. As expected, the weaker stratification cases take longer to return to the equilibrium position. In the case of Stokes flow (figure 5.9), particles are displaced further from the equilibrium position for all stratification cases and take longer to restratify.

Computing the mean fluid particle displacement as a function of body distance traveled shows the variation of fluid transport of a moving sphere in potential (figure 5.10) and Stokes (figure 5.11) flow. For the moving sphere in potential flow, the mean fluid particle displacement reaches an

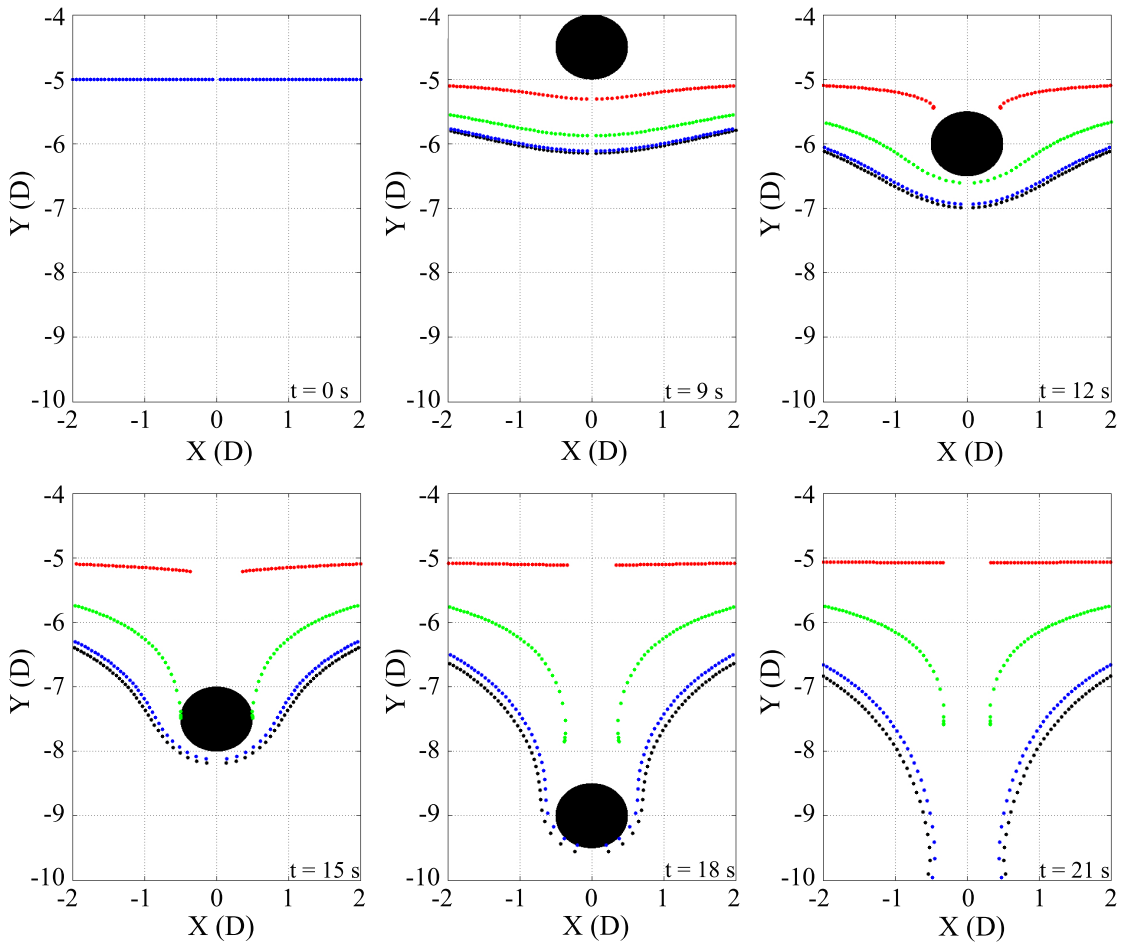

Figure 5.9. Displacement of fluid particles in Stokes flow due to a moving sphere. Black dots indicate fluid particles in unstratified flow conditions. Blue, green and red dots represent fluid particles in stratified flow with $N = 0.01$, $N = 0.1$, and $N = 1$ s^{-1}, respectively.

asymptotic value in the unstratified case; for Stokes flow, the mean displacement increases with time. These observations for mean particle displacement is synonymous to drift volume using asymptotic mathematical methods, where drift is finite and infinite in potential and Stokes flow, respectively [34, 41]. The maximum mean displacement ($\overline{X_{max}}$) is nearly increased by an order of magnitude between potential and Stokes flow for all stratification cases (see table 5.1). The time between the start of body motion and where mean fluid particle displacement reaches a maximum (defined as t_{max}) increases with decreasing N. Based on dimensional analysis, the long-term behavior of the mean particle displacement can be described as a decaying exponential function,

$$\overline{X_{stratified}} = C\, \exp\left(-B\, t\right), \tag{5.9}$$

where C is a constant with units of length, t is time and B is equivalent to the buoyancy frequency N. For potential flow with $N = 1$, $N = 0.1$ and $N = 0.01$ s^{-1}, the constant B is 0.94, 0.10 and 0.01 s^{-1}, respectively. We expect that the variation in time constants is due to the presence of the body as it moves past the plane of fluid particles. This effect is more prevalent as buoyancy frequency is increased. From inspection of figures 5.10 and 5.11, the time between the start of body motion and restratification of the flow (defined as t_{total}) increases by approximately an order of magnitude (in general) as N is decreased by an order of magnitude.

The effect of the body on fluid particle displacement as flow type and stratification are varied can be effectively described by close analysis of the ratio of stratified and unstratified mean fluid particle displacements (figure 5.12). The asymptotic behavior of the ratio decays slower for Stokes flow than potential flow for all stratification cases (figure 5.12A). The effect of the body results in a local minimum of the displacement ratio in potential flow (figure 5.12). Due to the lack of viscous boundary layer, particles located adjacent to the body as the body moves past the particle plane are transported backwards (upstream) by conservation of mass. The magnitude of this backwards motion (called reflux; [39]) is substantial such that the mean value of fluid particle displacement also becomes negative. For Stokes flow, reflux is not observed for all stratification cases. The reflux and recovery of particle positions (local maximum after local minimum associated with reflux) result

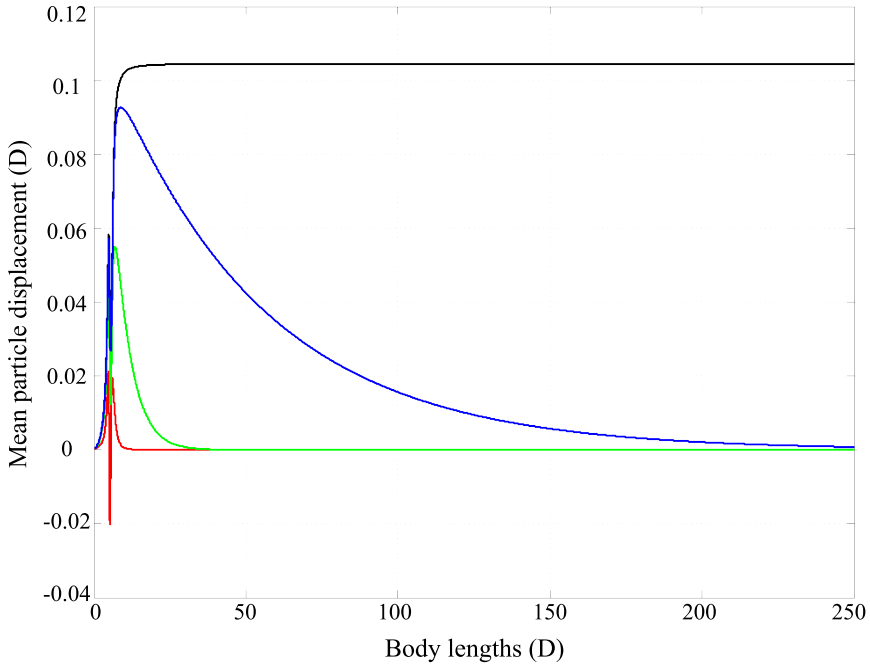

Figure 5.10. Mean displacement of fluid particles in potential flow for unstratified (black curve) and stratified conditions. Blue, green and red curves represent mean displacement in stratified flow with $N = 0.01$, $N = 0.1$, and $N = 1$ s^{-1}, respectively. Axes are in units of body diameters D.

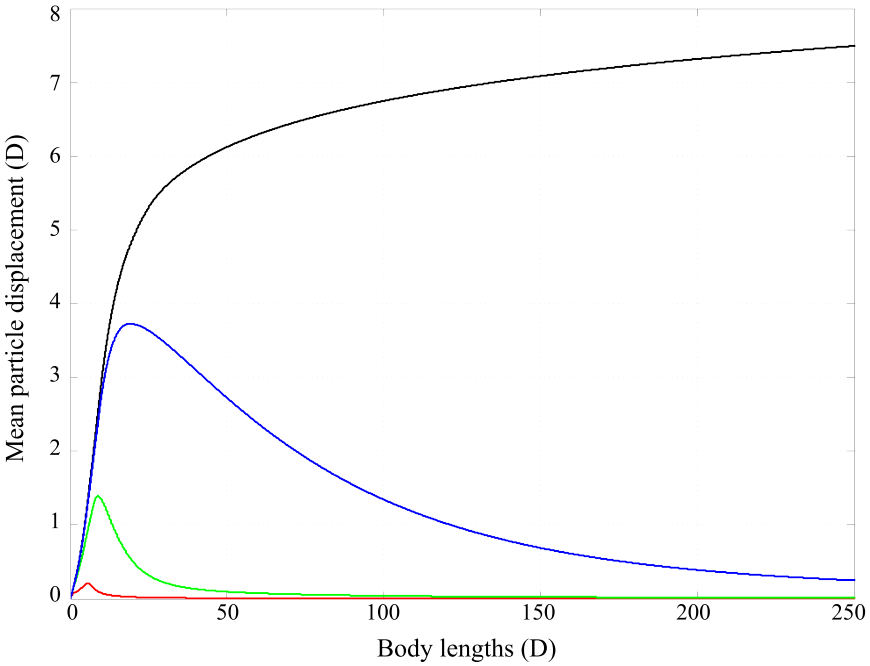

Figure 5.11. Mean displacement of fluid particles in Stokes flow for unstratified (black curve) and stratified conditions. Blue, green and red curves represent mean displacement in stratified flow with $N = 0.01$, $N = 0.1$, and $N = 1$ s^{-1}, respectively. Axes are in units of body diameters D.

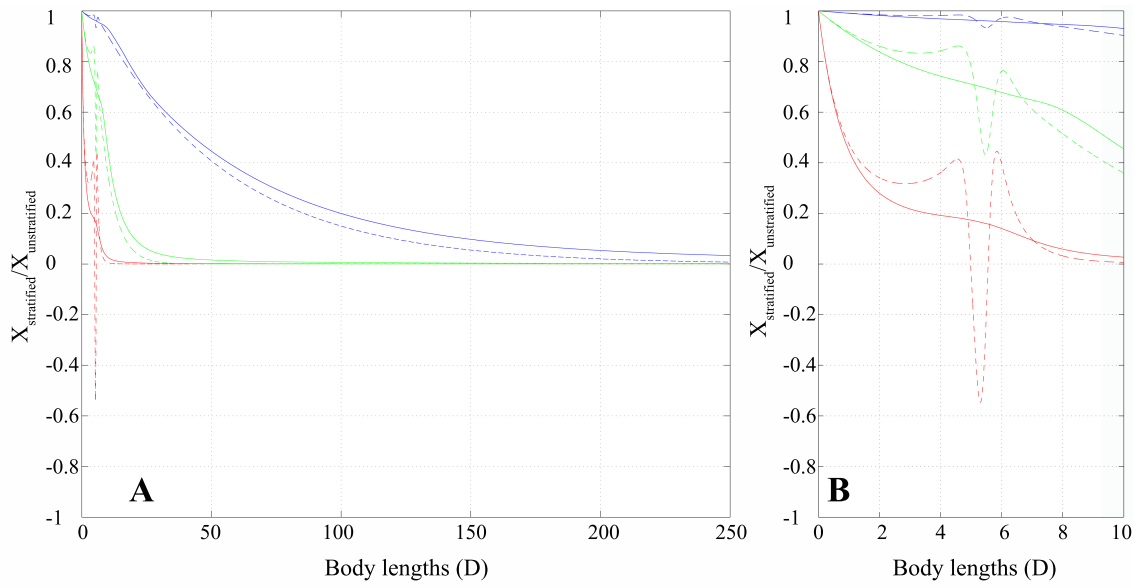

Figure 5.12. Comparison of normalized fluid particle mean displacement in potential (dashed curves) and Stokes (solid curves) flow for unstratified (black curves) and stratified conditions. Blue, green and red curves represent mean displacement in stratified flow with $N = 0.01$, $N = 0.1$, and $N = 1$ s^{-1}, respectively. A, Asymptotic behavior of normalized mean displacement. B, Behavior of normalized fluid particle mean displacement before, during and after body passes equilibrium position of particles.

in the variation of time constant B from the buoyancy frequency N (in equation (5.9)) for the asymptotic behavior.

Assuming that the body size D and swimming speed U for the sphere in the simulations are 10 cm and 5 cm s^{-1}, values for maximum mean displacement ($\overline{X_{max}}$) of fluid particles, time to maximum displacement (t_{max}), and restratification (t_{total}) can be estimated (summarized in table 5.1). The values of t_{total} in table 5.1 correspond to when the difference in mean displacement becomes less than 10^{-8} cm. The ratio between the drift volume (V_D) and the displaced drift volume due to diffusion (V_{DD}) as a function of t_{max} ($V_{DD}/V_D\,(t_{max})$) and t_{total} ($V_{DD}/V_D\,(t_{total})$) are also included in table 5.1 and discussed in section 5.4.

5.4 Discussion

To determine if diffusion alone can mix the stirring induced by drift before restratification, a diffusive time scale for the flow needs to be quantified. By dimensional analysis, the diffusive time scale (t_{diff})

Table 5.1. Summary of numerical simulation results. The duration between simulation initialization and time at which the mean fluid particle displacement attains the maximum value ($\overline{X_{max}}$) is denoted by t_{max} (second column). The time between simulation initialization and all fluid particles returning to their equilibrium position is denoted by t_{total} (fourth column). Approximate values represent uncertain quantities due to limited computational resources. The ratio between the drift volume (V_D) after diffusion reduction (V_{DD}) volume (computed from equation (5.11)) as a function of t_{max} ($V_{DD}/V_D\,(t_{max})$) and t_{total} ($V_{DD}/V_D\,(t_{total})$) are shown in columns five and six, respectively; these quantities are discussed in section 5.4.

	t_{max} [s]	$\overline{X_{max}}$ [cm]	t_{total} [s]	$V_{DD}/V_D\,(t_{max})$ [%]	$V_{DD}/V_D\,(t_{total})$ [%]
Potential					
N=1	12.04	0.20	45.08	10.33	19.47
N=0.1	13.89	0.55	106.00	11.06	29.00
N=0.01	17.80	0.93	636.80	12.48	62.26
Stokes					
N=1	11.39	2.10	286.30	10.05	45.03
N=0.1	17.80	13.93	295.70	12.48	45.66
N=0.01	38.37	37.27	1015.56	18.04	73.69

is

$$t_{diff} \sim \frac{1}{k_T}\left(\frac{L}{2}\right)^2, \tag{5.10}$$

where k_T is the thermal diffusivity of seawater ($k_T = 1.46 \times 10^{-7}$ m^2 s^{-1}) and L is the characteristic length scale of the flow (chosen as sphere diameter D). Given these parameters, the diffusive time scale is found to be on the order of 10^4 s. For potential and Stokes flow with buoyancy frequency $N = 0.01$ s^{-1}, the time at which stirring occurs before restratification is on the order of 10^3 s. Hence, the diffusion time scale is longer than the time scale associated with drift. Therefore, in order for the stirred fluid (via animal-induced drift) to fully mix, mixing processes in addition to diffusion are required to act on the drift volume.

Despite this conclusion, it is useful to consider the fraction of fluid that becomes permanently displaced due to diffusion. By constraining diffusion to act on the drift volume boundary (or interfacial regions), we can approximate the volume of fluid that sloughs off the drift volume (which is permanently displaced), while the remaining fluid returns to the equilibrium position [81, 109]. After a time specified by t, an amount of fluid characterized by the penetration depth l_{diff} has diffused to the surrounding ambient temperature (figure 5.13). Using the relationship in equation (5.10), the diffusion penetration depth can be found. By approximating the drift volume as a

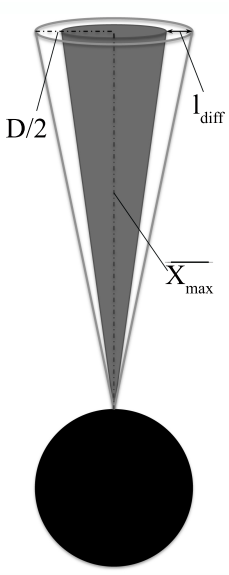

Figure 5.13. Diagram depicting the diffused drift volume. The total drift volume is approximated by a cone and outlined by the gray lines, with radius and height of $D/2$ and $\overline{X_{max}}$, respectively. The diffused drift volume is the solid conical volume, whose base radius is less than the drift volume by the penetration depth l_{diff}.

cone with base and height characterized by the body diameter D and maximum mean particle displacement $\overline{X_{max}}$, respectively, the drift volume that becomes permanently displaced due to diffusion is $V_{DD} \approx V_D - \frac{\pi}{3}\left(D/2 - l_{diff}\right)^2 \overline{X_{max}}$. To compare the diffused drift volume with the original drift volume, the diffusion drift ratio is defined as

$$\frac{V_{DD}}{V_D} = 1 - \frac{\left(D/2 - 2\sqrt{k_T\, t}\right)^2}{\left(D/2\right)^2}. \tag{5.11}$$

Selection of $t = t_{max}$ and $t = t_{total}$ will underestimate and overestimate the diffused drift volume, respectively. Values of diffusion drift ratio corresponding to t_{max} and t_{total} are summarized in table 5.1 for potential and Stokes flow.

The drift volume that is permanently displaced via diffusion ranges from 10% to 50% of the drift volume in unstratified flow conditions (table 5.1, fifth and sixth columns). To infer global input of biogenic mixing in a stratified environment, we will refer back to equation (4.3) and use the conservative estimate for the diffused drift volume in potential flow ($\frac{V_{DD}}{V_D} \approx 0.1$). Given the definition of diffused drift volume ratio in equation (5.11) we can rewrite the numerator of equation (4.3) (the

mixing energy due to drift) in terms of the diffused drift volume (V_{DD}),

$$(V_{DD})^{2/3}\,\frac{U^3}{L^2} = \left(\frac{V_{DD}}{V_D}\right)^{2/3}\left[(V_D)^{2/3}\,\frac{U^3}{L^2}\right], \tag{5.12}$$

where the second quantity in parentheses on the right of the equality represents the mixing energy due to drift in an unstratified flow. Therefore, the range of total mixing energy due to the diffused drift volume is on the order of 10^{-5}–10^{-6} W kg^{-1}. These values are an order of magnitude less than those reported for drift mixing energy in an unstratified fluid (section 4.4).

Based on the estimate of total global energy input of biomixing (10^{12} W) and the range of the estimated drift mixing energy in an unstratified flow (resulting from equation (5.12)), we approximate the total biomass in the ocean to be on the order of 10^{16}–10^{17} kg. Using the estimate for biomixing from the diffused drift volume and the ocean biomass, we find that the total global energy input to mixing via diffusion of the drift volume alone is on the order of 10^{11} W. Although this value is less than the value reported for drift in unstratified flow [67], the contribution to mixing in the oceans by swimming animals is not negligible since contributions to mixing by physical mixing sources are of the same order [89, 141, 2, 142]. However, we note that these values underestimate what we would expect for real dynamics, since the approximation of the drift volume as a cone is less than the actual drift volume for viscous flows (see figure 5.9). In addition, these estimates are based on the fluid transport of a single animal; transport may be enhanced by the presence of neighboring animals in a school (section 4.4).

Biogenic mixing via stirring may initiate double-diffusive processes in the ocean, thereby enhancing mixing in the ocean. While double-diffusive mixing processes are not considered a major contributor to the energy budget for ocean mixing (such as winds, tides and internal waves), the resultant fluid displacement from animal-induced drift is dynamically similar. Since double-diffusive processes are prevalent in the ocean and occur in regions where we would expect biogenic mixing to occur (discussed in more detail below), further inspection into whether swimming motions can lead to double-diffusive mixing is warranted. The density ratio R_ρ is used to determine whether

double-diffusive processes occur,

$$R_\rho = \frac{\alpha \Delta T}{\beta \Delta S}, \tag{5.13}$$

where α and β are the thermal expansion and salinity contraction coefficients, respectively, and T and S are temperature and salinity [110]. The Δ symbols denote variations in quantities with depth. If $R_\rho < 0$, the fluid is said to be stable; if $0 < R_\rho < 1$, then the flow exhibits diffusive convection [119, 130]. Diffusive convection occurs when cold, fresh water lies above warm, salty water. If fluid is displaced downwards (for example), the colder water warms faster than the salinity changes and returns to the initial location faster than it was displaced, resulting in oscillatory motions of the fluid parcel. If $1 < R_\rho < 100$, salt fingering occurs [60, 107]. Salt fingering is initiated when warm, salty water lies above cold, fresh water. As a parcel of fluid is displaced downwards (or upwards), the temperature of the fluid parcel cools (or warms). Because heat diffuses faster than salt, the density of the parcel increases (or decreases) leading to further displacement of the fluid parcel. The intensity of salt fingering is a strong function of the density ratio with theory estimating that it should be strongest as $R_\rho \to 1$ [109]. Measurements in the field and laboratory indicate maximal growth rates of fingers for density ratios less than 2 [72, 73].

Given these limits on R_ρ, we find that in regions where we would expect biogenic mixing to occur (i.e., marine lakes in Palau), conditions for double-diffusive processes are supported (figure 5.14). Based on five CTD casts in Jellyfish Lake during November 2008, temperature and salinity profiles with depth reveal a region where both profiles increase over the same depth (figure 5.14A). From equation (5.13), the variation of density ratio with depth is determined (figure 5.14B). Between 1 and 6 m, we find R_ρ values characteristic of diffusive convection. This region happens to coincide with the daytime location of migrating *Mastigias sp.* [56].

Finally, we consider whether animal-induced drift of fluid may initiate double diffusive processes. Since diapycnal mixing requires permanent vertical displacement of fluid parcels, we focus our efforts on salt fingering since diffusive convection results in the oscillation of fluid parcels around an initial position. The width of salt fingers (often a few centimeters in size) are on the scale of many swimming animals such that direct interaction of biota with salt fingers may be possible. From simulations of

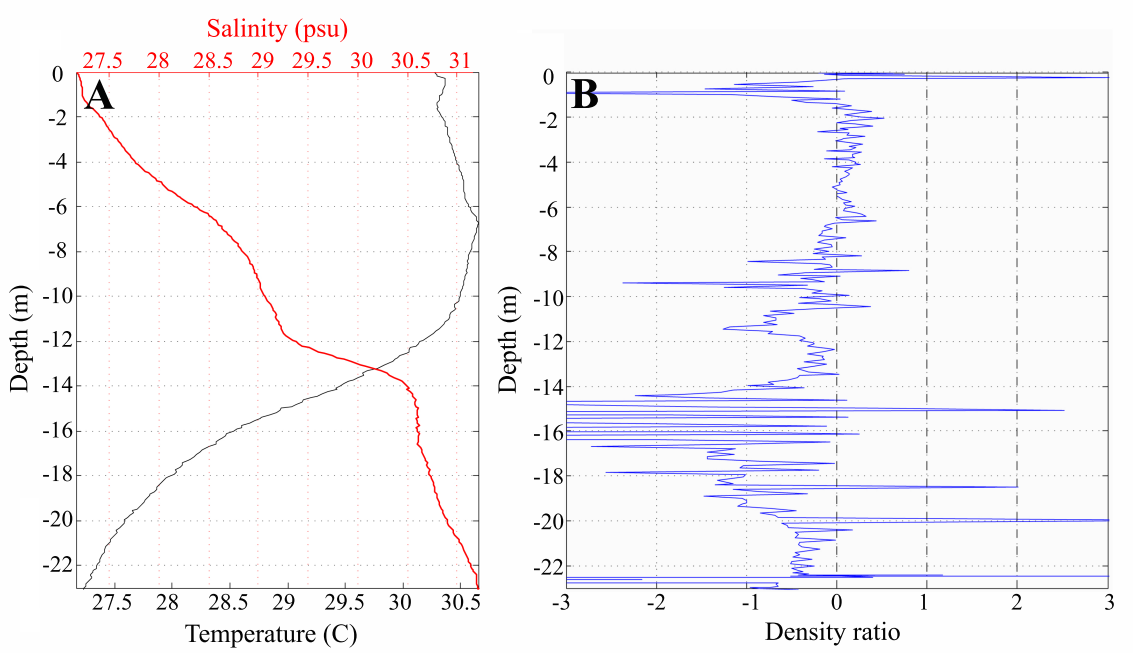

Figure 5.14. Physical properties of Jellyfish Lake in Palau measured from five CTD profiles. A, Profiles of temperature and salinity with depth of the marine lake. B, Based on profiles in A and the definition of R_ρ in equation (5.13), the variation of R_ρ with depth is shown. Black dashed lines indicate measured limits of diffusive convection ($0 < R_\rho < 1$) and salt fingering ($1 < R_\rho < 2$).

drift, we have shown that a body translating in a flow transports fluid in the direction of body motion, whose extent is limited by stratification (figures 5.10 and 5.11), inertial effects (figure 4.5A), and body shape (figure 4.5B). Despite these limitations, drift still results in the non-zero displacement of fluid. If a single animal is vertically migrating downwards in a region where salt fingering is favorable, drifting fluid behind the animal will cause stirring of warm, salty fluid into cold, fresh fluid. As the stirred fluid is warmed via diffusion, the temperature gradients will no longer offset the salinity gradients, initiating salt fingering and additional downward transport of fluid independent of the swimming animal.

On a larger scale, we consider conditions where vertically migrating behavior of entire animal populations have the ability to initiate salt fingering. As mentioned previously, the measured maximal growth rates for salt fingering correspond to $R_\rho < 2$ [73]. Conditions favorable to salt fingering have been documented in the Atlantic and Indian Oceans and most central waters [61, 109], which are coincidentally locations for low productivity because of limited nutrient supply [35]. Nearly 95%

of the upper kilometer in the mid-Atlantic is fingering favorable, with more than 65% of that region having a density ratio between 1.5 and 2.5 [108]. Therefore, to initiate aggressive, fast salt fingering processes, the density ratio must be reduced to the measured maximum limit of 2 [72]. Based on the definition of density ratio (equation (5.13)), R_ρ can be reduced if ΔT or ΔS is decreased or increased, respectively. Since we want to investigate the onset of salt fingering due to biogenic mixing separate from other sources, we neglect sources of T and S. Therefore, given these limitations, ΔS cannot increase by biogenic mixing alone; decreasing ΔT by biogenic transport is possible. When a large population of swimming animals vertically migrate, we expect a larger contribution of fluid transport compared with a single animal. As the vertical migration of animals continue, the stirred fluid due to their motions will diffuse to the ambient fluid properties, decreasing the gradients of temperature over time. If the temperature gradient is changed such that it no longer offsets the salinity stratification, salt fingering will occur [109, 73]. It remains to be shown both experimentally and theoretically the limits that will allow for initiation of salt fingering by biogenic mixing.